# Stratigraphy of hydrated sulfates in the sedimentary deposits of Aram Chaos, Mars

Kimberly A. Lichtenberg,[1] Raymond E. Arvidson,[1] Richard V. Morris,[2]
Scott L. Murchie,[3] Janice L. Bishop,[4] David Fernandez Remolar,[5] Timothy D. Glotch,[6]
Eldar Noe Dobrea,[7] John F. Mustard,[8] Jeffrey Andrews-Hanna,[9] and Leah H. Roach[8,10]

[1]   Sedimentary deposits within the 280 km wide crater containing Aram Chaos (~3°N, 339°E) have been differentially eroded by wind to expose a stratigraphic column 900–1000 m thick that unconformably overlies the chaos bedrock. A detailed stratigraphic and mineralogical description of the deposits is presented based on data from the Mars Reconnaissance Orbiter Compact Reconnaissance Imaging Spectrometer for Mars, Context Imager, and High Resolution Imaging Science Experiment. Two sedimentary units overlie the basement chaos material representing the original plains fill in Aram Crater: the first and oldest is composed of (1) a 50–75 m thick dark-toned basal unit containing ferric hydroxysulfate intercalated with monohydrated-sulfate-bearing materials, (2) a 75–100 m thick light-toned unit with monohydrated sulfates, and (3) a 175–350 m thick light-toned resistant capping unit with nanophase ferric oxides and monohydrated sulfates. After a period of wind erosion, these deposits were partially and unconformably covered by the second sedimentary unit, a 75–100 m thick, discontinuous dark-toned unit containing crystalline hematite and polyhydrated sulfate material. These sedimentary deposits were formed by evaporite deposition during at least two distinct rising groundwater episodes fed by regional-scale recharge. Later groundwater event(s) formed the polyhydrated materials, indicating that environmental conditions changed to a higher water-to-rock ratio. Wind has continued to shape the landscape after the last wetting event to produce the features and exposures observed.

## 1. Introduction

[2] The discovery from orbit of layered sedimentary hydrated sulfate deposits in analyses of Mars Express Observatoire pour la Minéralogie, l'Eau, les Glaces et l'Activité (OMEGA) data [*Gendrin et al.*, 2005; *Arvidson et al.*, 2006], subsequently confirmed and extended in analyses of Mars Reconnaissance Orbiter (MRO) Compact Recon-

naissance Imaging Spectrometer for Mars (CRISM) data [*Murchie et al.*, 2009; *Roach et al.*, 2009], has revolutionized our understanding of the evolution of Mars. The measurements obtained by the Mars Exploration Rover Opportunity during its exploration of the top of a thick sequence of sulfate-rich deposits in Meridiani Planum provide a detailed view of the depositional environment of these types of deposits. Specifically, results point to an acid-sulfate-dominated lacustrine system alternating with more arid conditions in which aeolian deposits accumulated [*Squyres et al.*, 2004; *Grotzinger et al.*, 2005; *Tosca and McLennan*, 2006]. With continued groundwater rise on a regional level the deposits were cemented and preserved [*Arvidson et al.*, 2006; *Andrews-Hanna et al.*, 2007].

[3] In this paper we build on previous studies of Aram Chaos [*Gendrin et al.*, 2005; *Glotch and Christensen*, 2005; *Massé et al.*, 2008b; *Noe Dobrea et al.*, 2008] by contributing (1) detailed mapping of the layered deposits using a combination of MRO Context Imager (CTX) with 5 m/pixel data [*Malin et al.*, 2007], High Resolution Imaging Science Experiment (HiRISE) data with 0.31 m/pixel observations [*McEwen et al.*, 2007], Mars Orbiter Laser Altimeter (MOLA) data at ~465 m/pixel [*Smith et al.*, 2001], and Mars

[1]McDonnell Center for the Space Sciences, Department of Earth and Planetary Sciences, Washington University, Saint Louis, Missouri, USA.
[2]NASA Johnson Space Center, Houston, Texas, USA.
[3]Johns Hopkins University Applied Physics Laboratory, Laurel, Maryland, USA.
[4]SETI Institute, Mountain View, California, USA.
[5]Centro de Astrobiología, INTA-CSIC, Madrid, Spain.
[6]Department of Geosciences, State University of New York at Stony Brook, Stony Brook, New York, USA.
[7]Planetary Science Institute, Tucson, Arizona, USA.
[8]Department of Geological Sciences, Brown University, Providence, Rhode Island, USA.
[9]Department of Geophysics, Colorado School of Mines, Golden, Colorado, USA.
[10]Now at Frontier Technology, Inc., Beverly, Massachusetts, USA.
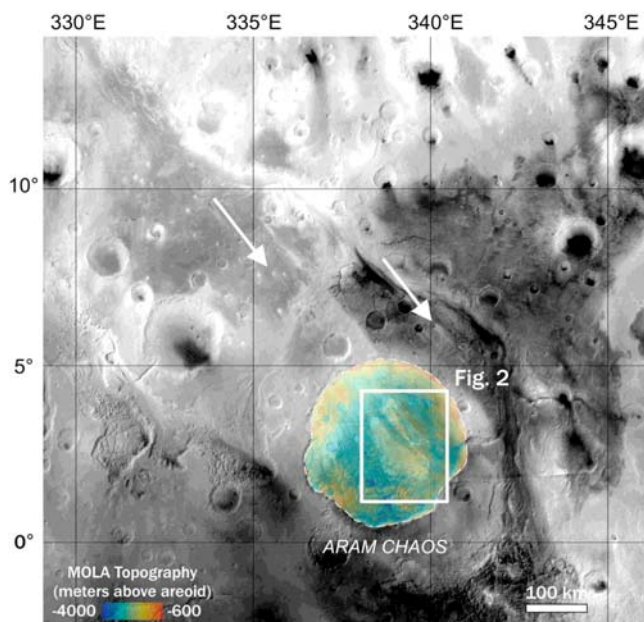
**Figure 1.** MOC-based mosaic of northern Xanthe Terra (231.55 m/pixel). White arrows indicate small craters with wind streaks trending to the southeast, showing the dominant wind direction in this area. The sedimentary unit within Aram Chaos is located in the white box; this is also the area shown in Figure 2. Other chaos regions can be seen to the west and south of Aram Chaos.

Express High Resolution Stereo Camera (HRSC) topographic data at 75 m/pixel [*Neukum et al.*, 2004] and (2) retrieval of mineral compositions for the stratigraphic units using CRISM hyperspectral targeted mode observations at ~20 and 40 m/pixel [*Murchie et al.*, 2007]. For reference, Figure 1 presents a regional-scale view of Aram Chaos, Figure 2a shows results from mapping mineralogy from OMEGA and TES data, and Figure 2b shows detailed mapping that we have done using the high-resolution CRISM observations. Figure 3 summarizes the key stratigraphic and mineralogic relationships developed in this paper, including the first identification on Mars of the ferric hydroxysulfate-Fe(OH)SO$_4$-located at and near the contact between the sedimentary deposits and the underlying chaos bedrock surface.

## 2. Geologic Setting

[4] Aram Chaos (~3°N, 339°E), contained within a 280 km wide crater of Noachian age, is one of a number of chaotic regions located in Xanthe Terra. Chaos terrain is characterized by a series of plateaus and mesas separated by

valleys that form a mosaic pattern (Figure 1) [*Rodriguez et al.*, 2005]. The likely chaos formation mechanism involved catastrophic outflow of pressurized groundwater, either through melting of subsurface ice or liquefaction [*Carr*, 1979; *Nummedal and Prior*, 1981; *Rodriguez et al.*, 2005]. The outflow of water that created the sunken chaos blocks also carved the channel on the east side of the crater and then joined other material flowing north in Ares Vallis [*Nummedal and Prior*, 1981]. After the initial chaos-forming event(s), subsequent aqueous activity in the area changed from erosion to deposition, producing the layered sedimentary materials that unconformably overlie the chaos bedrock materials [*Glotch and Christensen*, 2005; *Oosthoek et al.*, 2007]. At some point postdeposition the area experienced an uplift, creating a domical structure within Aram Crater [*Glotch and Christensen*, 2005; *Oosthoek et al.*, 2007; *Massé et al.*, 2008b]. The layered deposits have experienced significant differential wind erosion, revealing stratigraphic layers of differing morphology, thermal inertia, and mineral composition (including gray crystalline hematite, nanophase ferric oxides (npOx), and hydrated sulfates materials) [*Gendrin et al.*, 2005; *Glotch and Christensen*, 2005; *Glotch and Rogers*, 2007; *Massé et al.*, 2008b; *Noe Dobrea et al.*, 2008]. The erosion was driven by winds trending from the northwest which formed elongated plateaus of partially eroded sedimentary materials running NW-SE (Figures 1 and 2) [*Oosthoek et al.*, 2007]. As noted by *Fenton and Richardson* [2001], wind directions have been to first-order invariant as Mars has moved through its orbital oscillations. Thus, these northwesterly winds have been active for a large fraction of geologic time.

## 3. Methodology

### 3.1. Orbital Data Sets

[5] We use an integrated data processing and geographic information system (GIS) approach using both ENVI and ArcMap commercial software packages. MOLA and HRSC topographic data, CTX images, and HiRISE images over the study area were map projected to an equidistant cylindrical (equirectangular) projection using a Mars radius of 3396.0 km (scales for each data set were commensurate with their intrinsic spatial resolution). The data sets were then incorporated into an ArcMap pyramid-structured database, which allowed covisualization of the all data sets with user-selected transparency values. CRISM data (observation footprints, false-color images, and mineral detections) were added to the GIS system, and the combination of the spectral processing capability of ENVI and the map capabilities of ArcMap was used to map superposition and embayment relationships, morphologic characteristics, and mineral

**Figure 2.** The extent of the layered sedimentary deposits in Aram Chaos is illustrated in these CTX-based mosaics. (a) Locations of OMEGA and morphologically identified extents of monohydrated and polyhydrated sulfates. CRISM targeted observations are indicated with white outlines; locations of Figures 6a, 6b, and 10 are indicated with yellow boxes. (b) Same area as Figure 2a but with CRISM-based mineral detections. Key is as follows: 1.9 and 2.4 $\mu$m absorptions indicative of polyhydrated sulfates (red), 1.9 $\mu$m absorption indicating enhanced hydration but without a corresponding 2.4 $\mu$m absorption indicating hydrated sulfate (light red), 2.1 and 2.4 $\mu$m absorptions indicative of monohydrated sulfates (blue), 2.23 $\mu$m absorption indicative of ferric hydroxysulfates (green). The cross section in Figure 3 is indicated by the white line (A to A').
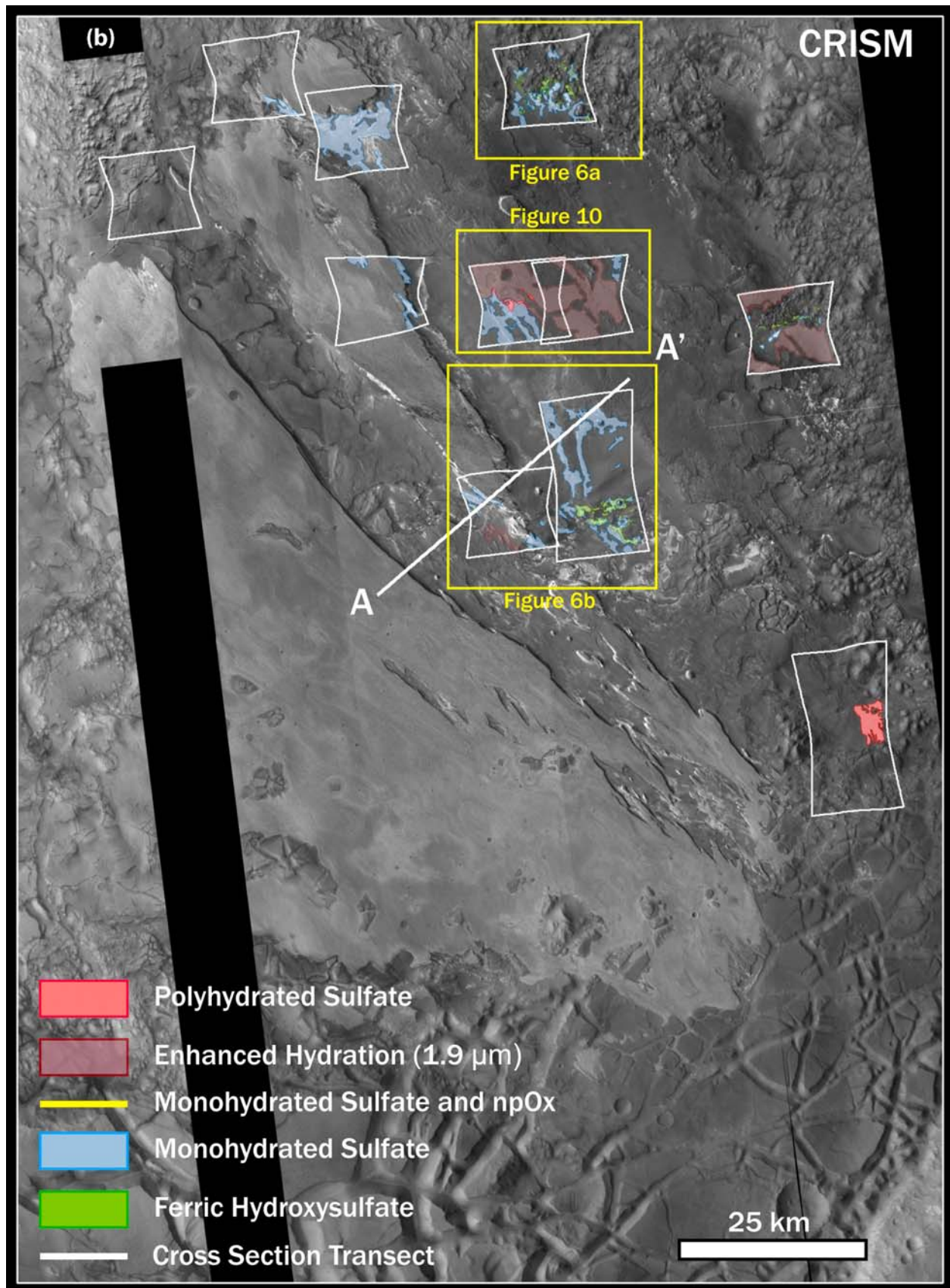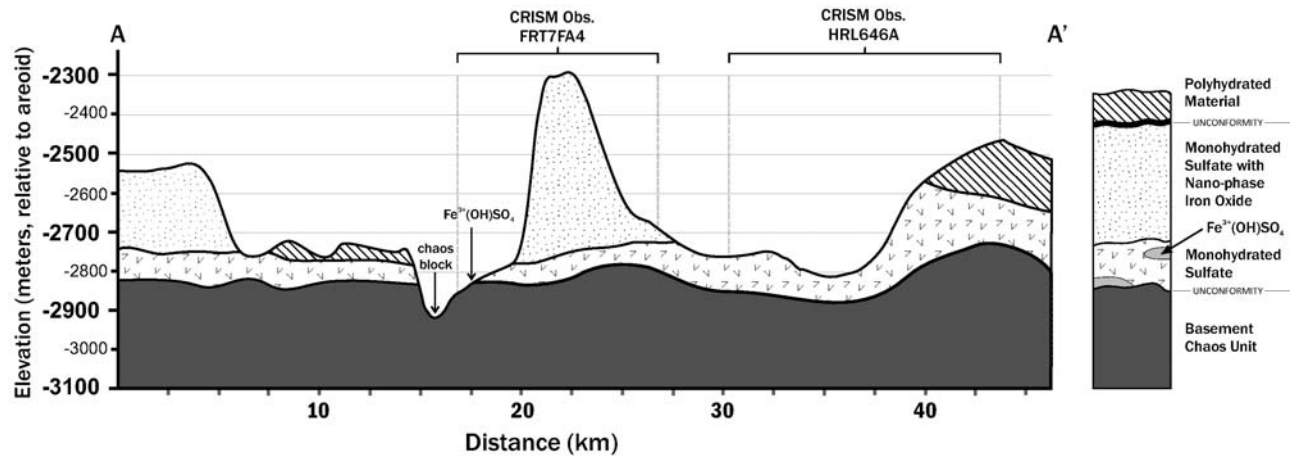
**Figure 2**

**Figure 2.** (continued)

**Figure 3.** Schematic cross section derived from mineralogic, morphologic, and topographic data and covering all described units of the sedimentary deposit. MOLA elevations are in meters below reference areoid. The monohydrated sulfate and ferric hydroxysulfate are shown in the stratigraphic column as discrete deposits, but the contact between them is likely gradational. On the other hand, the boundary with the polyhydrated material is an unconformity separated by a period of erosion.

inferences of the various layered units superimposed on the basement chaos materials.

[6] CRISM is a hyperspectral imager that can acquire up to 544 spectral channels between 0.39 to 3.9 $\mu$m with two detectors: a short-wavelength detector that functions between 0.39 and 1.04 $\mu$m (S detector) and a long-wavelength detector that functions from 1.0 to 3.9 $\mu$m (L detector) [*Murchie et al.*, 2007]. CRISM has two operational modes: a hyperspectral targeted mode (FRT, HRL, and HRS) and a multispectral nadir-looking mode (MSP). The multispectral mode is designed to provide mineralogical information for as much of the surface as possible, whereas the hyperspectral mode is designed to probe the mineralogy of relatively small areas in great detail. In the hyperspectral mode, gimbaling allows the instrument to be pointed at specific locations to the left or right of the spacecraft track while acquiring data at full spectral (544 bands, 0.39–3.9 $\mu$m) resolution and either full or half spatial resolution (~18 or ~40 m/pixel, respectively) [*Murchie et al.*, 2007]. Multiple images are taken on the incoming and outgoing spacecraft track to sample different path lengths through the atmosphere, but in this paper only the center observation is used. Targeted observations cover ~1300 km$^2$ of the sedimentary deposit in Aram Chaos.

[7] CRISM data presented in this paper were converted to I/F by dividing radiance on sensor by the solar radiance. Atmospheric gas band absorptions were removed by normalizing to a gas transmission spectrum. This spectrum, from data acquired over Olympus Mons where the surface spectra are dominated by dust signatures, is obtained by dividing I/F values at the base of Olympus Mons by values at the summit. The variation in atmospheric path length from the base to the top of the volcano provides a transmission spectrum which can then be used to remove gas features from other spectra. This method has been used extensively in reduction of hyperspectral data [*Langevin et al.*, 2005; *Mustard et al.*, 2005; *Lichtenberg et al.*, 2007], and here is applied to L detector data only because that is the spectral region in which atmospheric gas bands are present. At

wavelengths shorter than ~1 $\mu$m, atmospheric effects are dominated by aerosols and we did not correct for these effects. Both L and S detector observations were photometrically corrected by dividing by the cosine of the incidence angle for each observation. Spectra of candidate mineral locations were also divided by a spectrum from within the same CRISM data set that is spectrally neutral in order to suppress remaining instrument artifacts. Specifically, the denominator spectra were chosen from nearby regions that are spectrally flat between 1 and 2.5 $\mu$m. For reference, Figure 4 shows the end-member spectra for each of our units identified from CRISM data, along with the neutral spectra used to generated ratioed spectra. For comparison purposes, Figure 4 also presents the ratioed versions of the spectra along with laboratory analogs discussed in section 3.2.

[8] Initial mineral detections were made using CRISM summary products generated with the ENVI plug-in CRISM Analysis Tool (CAT) [*Pelkey et al.*, 2007]. The spectral parameter summary products take advantage of unique absorptions or combinations of spectral features that some minerals have in the visible/near-infrared wavelengths, and are a first-order tool for identifying locations to explore in greater detail with the full wavelength range of the data set. For example, most hydrated sulfates have a spectral feature at 2.4 $\mu$m [*Cloutis et al.*, 2006], and, therefore, a mathematical expression which takes into account the overall slope of the spectrum in that wavelength region and the actual absorption at 2.4 $\mu$m can be used to identify the possible signature of sulfates in a spectrum [*Pelkey et al.*, 2007]. Multiple parameters can be used together to identify monohydrated sulfates (absorptions at both 2.1 and 2.4 $\mu$m) or polyhydrated sulfates (absorptions at 1.4, 1.9, and 2.4 $\mu$m). Initial detections of hydrated minerals within the layered deposits were made over Aram Chaos using the spectral parameters or combinations of spectral parameters indicated in Table 1. A new parameter algorithm was developed after examination of both I/F and ratioed data showed the pres-
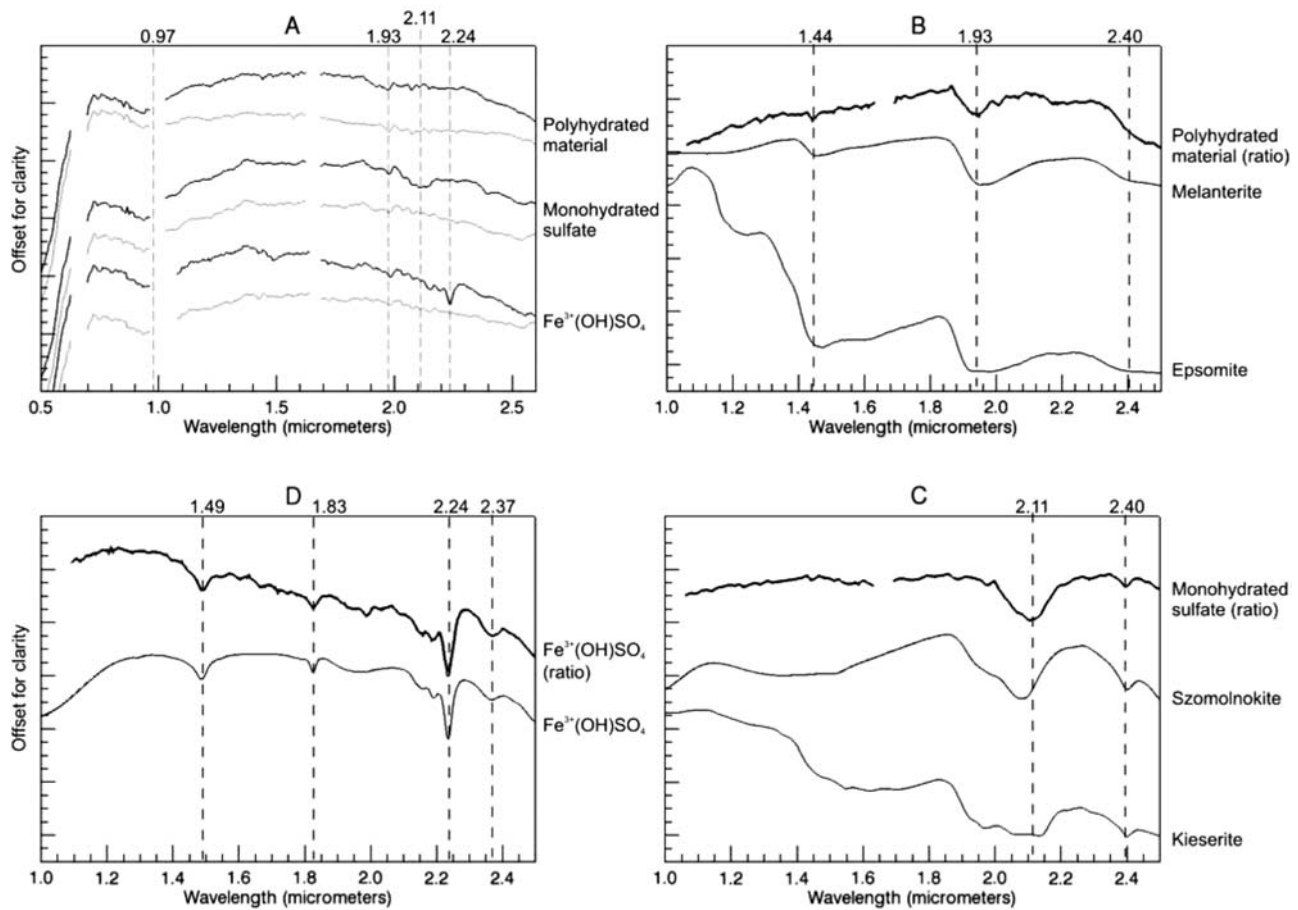
**Figure 4.** (a–d) Spectral reflectance characteristics of the sedimentary deposits. Wavelengths shorter than 1.0 $\mu$m are not shown for the ratioed spectra since there are no neutral spectra in this wavelength region. Spectra in Figure 4a are offset; spectra in Figures 4b, 4c and 4d are scaled and offset for clarity. Numbers above the plots are in micrometers and indicate indentifying absorptions. Figure 4a shows atmospherically and photometrically corrected numerator and denominator spectral pairs for the ferric hydroxysulfate, monohydrated sulfate, and polyhydrated sulfate; numerators are shown in black, and denominators are shown in gray from 0.5 to 2.5 $\mu$m. Data not shown at around 1.0 $\mu$m (detector boundary) and 1.65 $\mu$m (known instrument artifact). Figure 4b shows polyhydrated sulfate ratioed spectrum (numerator/denominator) and lab spectra for candidate minerals melanterite [$Fe(SO_4) \cdot 7H_2O$] and epsomite [$Mg(SO_4) \cdot 7H_2O$]. Figure 4c shows monohydrated sulfate ratioed spectrum and candidate minerals szomolnokite [$Fe^{+2}(SO_4) \cdot H_2O$] and kieserite [$Mg(SO_4) \cdot H_2O$]. The kieserite spectrum presented here may have water contamination as evidenced by the absorption at ~1.9 $\mu$m. Figure 4d shows ferric hydroxysulfate ratioed spectrum and laboratory-created ferric hydroxysulfate [$Fe(SO_4)OH$]; the CRISM band with the minimum around 2.24 $\mu$m is at 2.238 $\mu$m, which is the closest CRISM band to 2.4 $\mu$m. The melanterite, szomolnokite, and ferric hydroxysulfate spectra are from laboratory experiments presented in the text and are also shown in Figure 5; the epsomite and kieserite spectra are from the CRISM spectral library.

ence in some locations of a sharp and relatively deep band at 2.238 $\mu$m. The parameter to map the depth of this band was defined as follows:

$$BD2230 = 1 - \frac{R2.2318}{\left(0.468 \times \frac{(R2.2120 + R2.1988)}{2} + 0.532 \times \frac{(R2.2583 + R2.2517)}{2}\right)}$$

where $R(\lambda)$ is the reflectivity at wavelength $\lambda$. This band depth parameter (BD2230) is now incorporated into the spectral summary parameters in CAT versions 6.5 and higher.

[9] Detections of specific minerals were confirmed by examining the wavelength range between 0.4 and 2.6 $\mu$m of the atmospherically and photometrically corrected hyperspectral data over each detection and comparing the spectra to laboratory-based mineral spectra resampled to CRISM band passes in the visible NIR wavelength range. As already noted, Figure 4 presents I/F spectra for end-members retrieved from CRISM data, along with the spectrally "neutral" spectrum used to generate ratio presentations. Also shown in Figure 4 are ratioed data for the L detector spectral range and laboratory spectra of likely analogs. The end-

**Table 1.** Summary Parameter Mineral Indicators

| Material | Primary Indicators ($\mu$m) | Secondary Indicators ($\mu$m) |
|---|---|---|
| Monohydrated sulfate | 2.1 + 2.4 | |
| Polyhydrated mineral | 1.9 | 1.4 |
| Polyhydrated sulfate | 1.9 + 2.4 | 1.4 |
| Ferric hydroxysulfate | 2.238 (2.24) | 1.48, 1.82, 2.38 |

member spectra were extracted from the CRISM spectra by inspection of band parameter maps and detailed examination of a large number of I/F and ratioed spectra where parameter maps indicated a relatively high abundance of a given mineral species.

[10] The imaging and spectral data sets were used in tandem to generate maps that show the locations of mineral identifications with CRISM data (Table 2), mineral identifications with OMEGA and TES data from previous work, and geologic units that contain the specific mineral signatures (Figures 2a and 2b). Gridded global topography data from MOLA (1 m vertical resolution) [*Smith et al.*, 2003] and digital elevation maps generated from stereo HRSC data (20–100 m vertical resolution) [*Ansan et al.*, 2008] were used in conjunction with the other data sets to define embayment and superposition relationships among the various units and to define the map units and stratigraphic relationships shown in Figures 2b and 3.

### 3.2. Laboratory Measurements

[11] To support spectral identification of sulfate-bearing minerals, visible and near-infrared (VNIR), Mössbauer (MB), and powder X-ray diffraction (XRD) measurements were acquired for synthetic melanterite (FeSO$_4$·7H$_2$O; Fisher Scientific) heated in air at 80°C, 110°C, 130°C, 150°C, 200°C, and 240°C for 2, 3, 18, 21, 21, 18 h, respectively. An Analogue Spectral Devices FieldSpec RS[3] spectrometer with a Muglight option was used to obtain VNIR spectra at room temperature. Transmission Mössbauer spectra were obtained at room temperature with a Ranger Scientific spectrometer (Model MS-1200) using a $^{57}$Co(Rh) source and analyzed using the methods outlined by *Morris et al.* [2000]. The values of the doublet Mössbauer parameters isomer shift ($\delta = (\nu_1 + \nu_2)/2$) and quadrupole splitting ($\Delta E_Q = \nu_1 - \nu_2$) were calculated from the center positions ($\nu_1$ and $\nu_2$ with $\nu_2 > \nu_1$) of the two peaks. The value of $\delta$ is reported relative to the center position of the spectrum of

metallic iron foil at room temperature. A Scintag XDS 2000 X-ray diffractometer using CuK$\alpha$ radiation and a step size of 0.02° 2$\theta$ was employed to obtain X-ray diffraction powder patterns (~293 K). On the basis of XRD patterns, the powders obtained by thermal decomposition of synthetic melanterite at 80°C and 240°C are synthetic szomolnokite (FeSO$_4$·H$_2$O) and ferric hydroxysulfate (Fe(OH)SO$_4$), respectively. VNIR and MB spectra of the synthetic melanterite, szomolnokite, and ferric hydroxysulfate are shown in Figure 5. As will be shown in section 4, melanterite is an example of a polyhydrated phase that matches CRISM-based spectra and szomolnokite is a possible match for the monohydrated phase in Aram Chaos. Fe(OH)SO$_4$ can be identified as a specific phase based on detailed comparison of CRISM-based and our laboratory data, as shown in Figure 4.

## 4. Stratigraphy and Mineralogy of Sedimentary Deposits

[12] Two major stratigraphic units unconformably overlying the basaltic basement chaos terrain were mapped in detail as part of our work (Figures 2b and 3). The chaos terrain beneath and surrounding the sedimentary deposits was described elsewhere in detail and will not be covered in this paper [*Glotch and Christensen*, 2005; *Oosthoek et al.*, 2007; *Massé et al.*, 2008b; *Noe Dobrea et al.*, 2008]. CRISM spectra for the chaos surfaces are consistent with the presence of nanophase ferric oxides variably mixed with basaltic materials. Descriptions for the two overlying sedimentary units incorporate both the results of this study and previous work in this area and are described in this section from oldest to youngest. The areal extents of the units in CRISM and OMEGA/TES data are given in Table 3. As already noted, a schematic cross section showing the current topographic relationships of the sedimentary units and basement chaos materials is shown in Figure 3.

### 4.1. Ferric Hydroxysulfate, Monohydrated Sulfate, and Nanophase Ferric Oxide Unit

[13] The first of the two sedimentary units has three distinctly different stratigraphic horizons. From oldest to youngest these are monohydrated sulfates with ferric hydroxysulfate, monohydrated sulfates, and monohydrated sulfates with nanophase ferric oxides. The changing mineralogy represents a facies change and likely temporal evolution in the environments of deposition and/or alteration.

**Table 2.** CRISM Targeted Observations Used in This Paper[a]

| Observation ID | Type | Day of Year[b] | Center Latitude/Longitude | Ls |
|---|---|---|---|---|
| HRL0000646A | Half resolution long | 2007_169 | 2.99°N, 339.62°E | 259.9 |
| FRT00007FA4 | Full resolution targeted | 2007_274 | 2.91°N, 339.42°E | 323.3 |
| HRL000087E6 | Half resolution long | 2007_302 | 2.40°N, 340.21°E | 338.5 |
| FRT00008EB6 | Full resolution targeted | 2007_357 | 3.34°N, 340.08°E | 6.8 |
| FRT00009496 | Full resolution targeted | 2008_008 | 3.92°N, 338.82°E | 14.8 |
| FRT000098B2 | Full resolution targeted | 2008_020 | 3.92°N, 339.50°E | 20.1 |
| FRT0000AB75 | Full resolution targeted | 2008_126 | 3.66°N, 338.58°E | 67.6 |
| FRT0000C14E | Full resolution targeted | 2008_231 | 3.41°N, 339.12°E | 114.6 |
| FRT0000C815 | Full resolution targeted | 2008_259 | 3.41°E, 339.44°E | 127.6 |
| FRT0000D26B | Full resolution targeted | 2008_303 | 3.41°N, 339.59°E | 149.4 |

[a]Observations are listed in chronologic order.
[b]Date format is year_day.
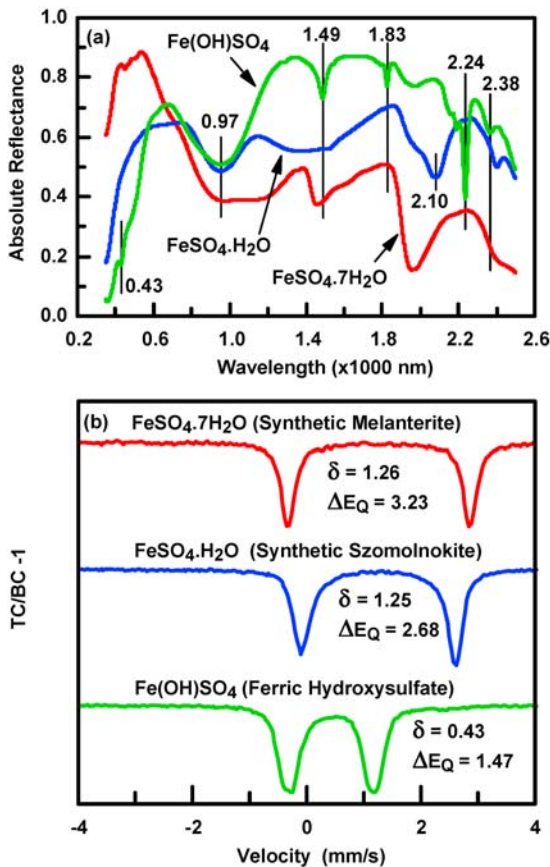
**Figure 5.** (a) VNIR and (b) Mössbauer spectra at room temperature for synthetic melanterite [$FeSO_4 \cdot 7H_2O$], szomolnkite [$FeSO_4 \cdot H_2O$], and ferric hydroxysulfate [$Fe(OH)SO_4$] were obtained by thermal decomposition of $FeSO_4 \cdot 7H_2O$ in air at 80°C and 240°C, respectively. For $Fe(OH)SO_4$ in Figure 5a, the spectral features at 1.49, 1.83, 2.24, and 2.38 $\mu$m are associated with $Fe^{3+}$-OH vibrations, and the spectral features at 0.43 and 0.97 $\mu$m are associated with $Fe^{3+}$ electronic transitions. The Mössbauer parameters ($\delta$ and $\Delta E_Q$) in Figure 5b are characteristic of octahedrally coordinated $Fe^{2+}$ ($FeSO_4 \cdot 7H_2O$ and $FeSO_4 \cdot H_2O$) and octahedrally coordinated $Fe^{3+}$ ($Fe(OH)SO_4$).

#### 4.1.1. Ferric Hydroxysulfate, Monohydrated Sulfates

[14] The sedimentary section sitting directly and unconformably on the chaos bedrock surface is spectrally dominated by monohydrated-sulfate-bearing materials, but together with ferric hydroxysulfate-bearing materials exposed in a number of areas (Figures 2b, 3, and 4). Examination of these exposures with HRSC DEM data shows that these deposits in total are 50 to 75 m thick. The $Fe(OH)SO_4$-bearing material occurs in small exposures that are intercalated with deposits of monohydrated sulfate (Figure 6). In the CRISM observations in which this signature is detected at the edge of the sedimentary deposit (FRT8EB6 and FRT98B2), the material is found in contact with both the basement chaos blocks and monohydrated sulfate (Figure 6a; FRT8EB6 not shown). In the CRISM observations over the interior of the sedimentary deposit (HRL646A and FRT7FA4; Figure 6b), the $Fe(OH)SO_4$ signature is only detected in areas where erosion has exposed the contacts between the sedimentary

material and the underlying basement chaos surfaces. Examination of HiRISE data (Figure 7) shows that areas with the $Fe(OH)SO_4$ signature correspond to dark material that is cracked on a several meter scale and superimposed by the light-toned, monohydrated sulfate-bearing material. Although the $Fe(OH)SO_4$-bearing unit occurs in only four of the targeted CRISM observations over Aram Chaos, areas with similar morphology in CTX data not covered by CRISM observations suggest that its occurrence is more extensive.

[15] The $Fe(OH)SO_4$ interpretation above is based on a spectral absorption at 2.238 $\mu$m, coupled with minor absorptions at 1.49, 1.82, and 2.38 $\mu$m (Figure 4). The 2.238 $\mu$m absorption is accompanied by a distinct spectral shape just shortward of 2.24 $\mu$m. The nondetection of a band centered at 1.40 $\mu$m indicates that structural $H_2O$ is not present at detectable levels. This material was previously mapped by both *Massé et al.* [2008b] and *Lichtenberg et al.* [2008] and interpreted to be an Al-OH bearing mineral by *Massé et al.* [2008a]. As noted previously in this paper, synthetic melanterite ($Fe^{+2}SO_4 \cdot 7H_2O$) was heated in laboratory air at ~240°C for 21 h, resulting in production of $H_2O$ and $H_2$ by-products, $Fe^{+3}$ from oxidation of $Fe^{+2}$, and formation of $Fe(OH)SO_4$. VNIR laboratory spectrum of the synthetic $Fe(OH)SO_4$ is shown compared to the ratioed CRISM spectrum of this material in Figure 4. Figure 5 shows the synthetic melanterite, szomolnkite, and ferric hydroxysulfate VNIR spectra along with Mössbauer spectra confirming the transition from $Fe^{+2}$ from synthetic melanterite to $Fe^{+3}$ as the sample was heated and converted to ferric hydroxysulfate. The VNIR spectra also show the shift of the ~1.9 $\mu$m absorption due to $H_2O$ in the melanterite to ~2.1 $\mu$m in the szomolnkite. The spectra of the ferric hydroxysulfate in Aram Chaos are similar to the spectra of dehydrated ferricopiapite reported by *Milliken et al.* [2008] and *Bishop et al.* [2009], although their data show neither an absorption at 1.82 $\mu$m nor the distinctive spectral structure shortward of 2.24 $\mu$m. The Aram Chaos ferric hydroxysulfate is also distinct from the ferric-bearing sulfates found at Gusev crater and Meridiani Planum on the basis of Mössbauer data (Figure 5 and *Morris et al.* [2006a, 2006b, 2008]).

#### 4.1.2. Monohydrated Sulfates

[16] Above approximately 75 m above the contact with the underlying chaos bedrock, the sedimentary deposit transitions without any major unconformities to a mono-

**Table 3.** Unit Characteristics

| Compositional Information | Extent of Coverage With CRISM Data | Extent of Coverage With OMEGA Data |
|---|---|---|
| polyhydrated sulfate[a]; crystalline hematite[b]; enhanced hydration; ferric oxides | 170 km$^2$ | ~2770 km$^2$ |
| nanophase ferric oxides; monohydrated sulfate[a] | - | 4600 km$^2$ |
| monohydrated sulfate[a] | 200 km$^2$ | ~1185 km$^2$ |
| ferric hydroxysulfate; monohydrated sulfate[a] | 18 km$^2$ | - |

[a]Also detected with OMEGA data.
[b]Detected with TES data [*Christensen et al.*, 2001; *Glotch and Christensen*, 2005].
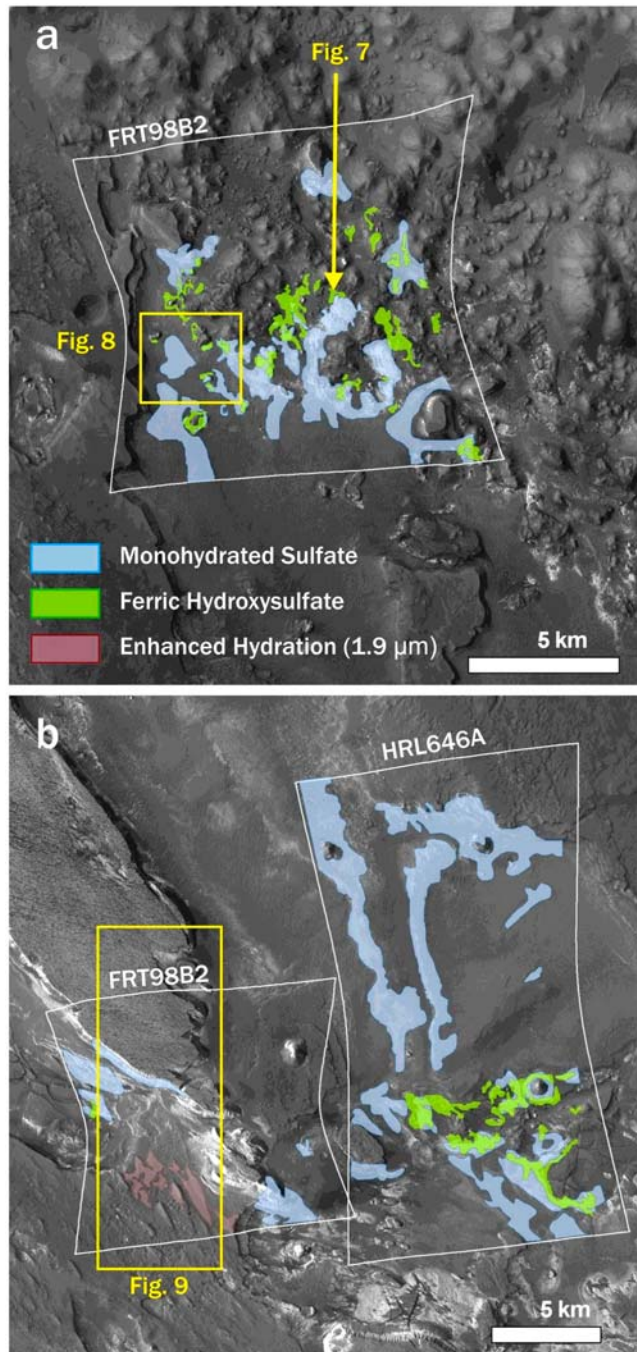
**Figure 6.** Locations of monohydrated sulfate (indicated by absorptions at 2.1 and 2.4 $\mu$m, shown in blue) and ferric hydroxysulfate (indicated by an absorption at 2.238 $\mu$m, shown in green) in three CRISM targeted observations. The location of Figure 7 is indicated by the yellow arrow. The locations of the HiRISE close-ups in Figures 8 and 9 are indicated with yellow boxes. (a) Monohydrated sulfate and ferric hydroxysulfate at the edge of the depositional unit. (b) Monohydrated sulfate and ferric hydroxysulfate in the interior of the sedimentary deposits where the deposits have been significantly eroded, exposing blocks of the chaos bedrock.

hydrated-sulfate-dominated material (Figures 2b, 3, and 4). This material, similar to the monohydrated sulfate signatures lower in the section, is characterized by spectral absorptions at ~2.1 and 2.4 $\mu$m and is dominated by flat, layered terrains with occasional scalloped textures due to wind erosion. This material is laterally extensive throughout the sedimentary deposit, covering approximately 1200 km$^2$. Although the spectral absorptions correspond most strongly with exposures of light-toned, scalloped material (Figure 7) the distinctive signatures are also apparent in flat-lying places of medium albedo (Figure 8). Based on examination of CTX data, these areas are most likely outcrops of the light-toned mono-hydrated sulfate-bearing material covered with a thin aeolian cover of basaltic sands [*Glotch and Christensen*, 2005]. The widespread but sporadic occurrence of this unit throughout the sedimentary deposit suggests it may be more common than indicated, but exposed by erosion only in certain places and obscured by basaltic sands in other locations. The total thickness of this monohydrated sulfate unit ranges from 75 to 100 m.

[17] *Gendrin et al.* [2005] identified this material as the magnesium monohydrated sulfate kieserite (Mg(SO$_4$)·H$_2$O) based on the lack of an Fe absorption between 0.6 and 1.0 $\mu$m. However, an absorption at ~1.0 $\mu$m in the nonratioed spectrum (Figure 4) suggests a possible iron-bearing sulfate such as szomolnokite, an interpretation that we prefer. The ferric hydroxysulfate that is spectrally a match to the material we see in Aram Chaos was formed by dehydration and oxidation of szomolnokite, lending credence to the presence of szomolnokite in the region.

### 4.1.3. Monohydrated Sulfates and Nanophase Ferric Oxides

[18] The monohydrated sulfate signature transitions to a cliff-forming section that attains a thickness of between 175 and 350 m and forms a capping plateau ~4600 km$^2$ in area, partially covered with basaltic sands. The exposed walls of this unit are light toned and indurated, with erosional scars down the sides where material has undergone gravity-
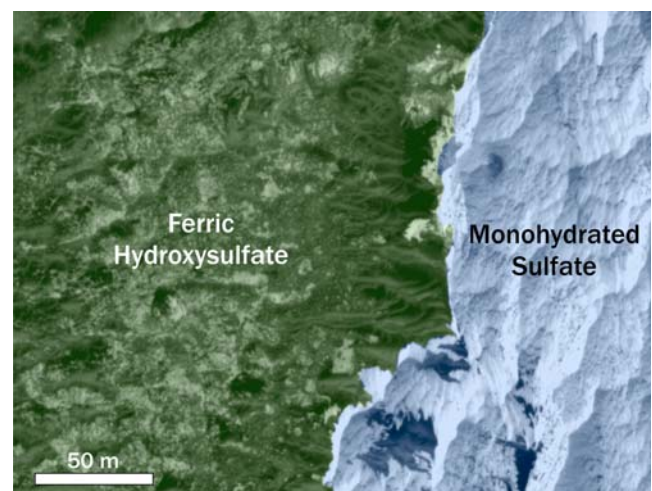


**Figure 7.** Subset of HiRISE image PSP_006953_1840 showing the contact between material exhibiting the mono-hydrated sulfates (light-toned scalloped area) and material showing absorptions indicative of the ferric hydroxysulfate (dark material).
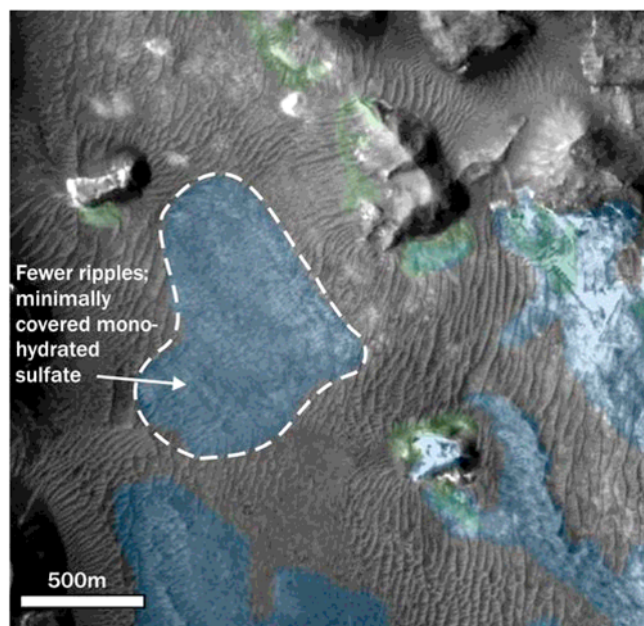
**Figure 8.** CTX mosaic over an area with strong 2.1 and 2.4 $\mu$m absorptions indicative of monohydrated sulfate. Blue shaded areas indicate the presence of monohydrated sulfate; green shaded areas indicate the presence of the ferric hydroxysulfate. Although most of the material that exhibits strong monohydrated sulfate signatures has a high albedo (Figure 7), the area enclosed by the dashed line does not, although some brighter material can be seen at the right edge. We interpret this to be an exposure of the monohydrated sulfate-bearing material in Figure 7 that is minimally covered with wind-blown sands.

induced slumping and sliding (Figure 9). Chaos bedrock can be seen as "kipukas" standing above and surrounded by these deposits in the southwest corner of Aram Chaos (Figure 2), and in certain places this material has been deeply eroded to reveal the basement chaos terrain [*Glotch and Christensen*, 2005]. The spectral signature of the light-toned cliffs is dominated by nanophase ferric oxides [*Morris et al.*, 2006a, 2006b; *Massé et al.*, 2008b], but minor absorptions at 2.1 and 2.4 $\mu$m indicate that the material also contains monohydrated sulfates [*Massé et al.*, 2008b].

[19] HiRISE images covering this unit (Figure 9) show that the exposed walls of this deposit are finely layered, with thicknesses similar to those inferred from the middle or monohydrated sulfate portion of the deposit. In fact, in CRISM observation FRT7FA4 up to twelve distinct layers are exposed within the monohydrated sulfate (middle) unit, forming a stair step pattern with some of the layers traceable to beneath the cliff-forming deposits.

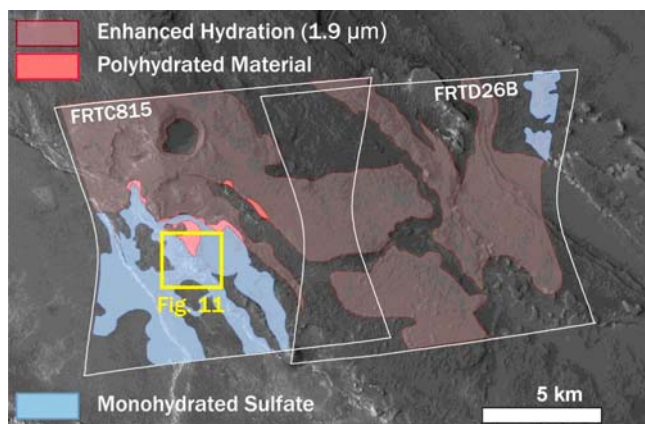## 4.2. Polyhydrated Sulfates, Hydrated Materials, and Hematite Deposits

[20] This second sedimentary unit is 75–100 m thick and is characterized by an absorption at 1.9 $\mu$m indicating the presence of one or more polyhydrated minerals and a plateau-like morphology. Compared to the monohydrated sulfates, the polyhydrated materials are darker and smoother and

appear more indurated and resistant to weathering than the monohydrated deposits. Previous work in Aram Chaos with OMEGA data has shown that one of the hydrated minerals is most likely a polyhydrated sulfate based on an additional absorption at 2.4 $\mu$m [*Gendrin et al.*, 2005; *Noe Dobrea et al.*, 2008]. Examination of the locations where the 1.9 $\mu$m band depth is present in CRISM data over the plateau (Figure 10) shows that polyhydrated minerals are present, but that their locations are not ubiquitous throughout the region as mapped by OMEGA (Figure 2a).

[21] This unit also coincides spatially with the detection of crystalline hematite, identified from Thermal Emission Spectrometer data [*Christensen et al.*, 2001; *Glotch and Christensen*, 2005; *Noe Dobrea et al.*, 2008]. Using OMEGA data *Massé et al.* [2008b] showed that goethite, ferrihydrite, or schwertmannite may also be present in this unit along with hematite. These ferric oxides are not expected to be stable under present-day Martian conditions;
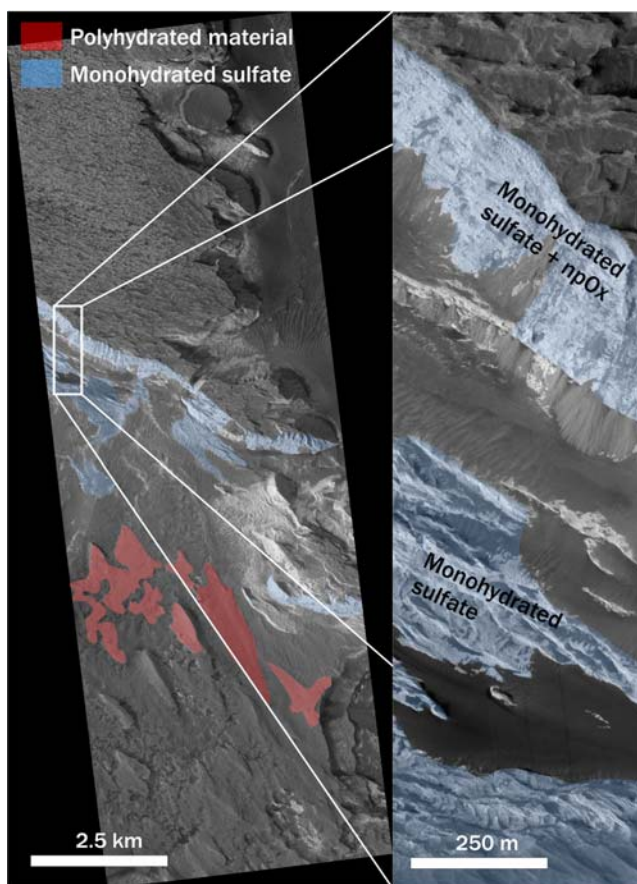


**Figure 9.** HiRISE image PSP_003406. The spectral signature of the walls is dominated by nanophase ferric oxides but also has faint absorptions at 2.1 and 2.4 $\mu$m indicating the presence of monohydrated sulfates. Locations of strong 2.1 and 2.4 absorptions (indicating the material is dominated by monohydrated sulfates) are shown here just below the cliff. The layered nature of both the monohydrated sulfate plus npOx material and the monohydrated sulfate material is visible in the blowup on the right. The outcrop of ferric hydroxysulfate in this area is not covered in this HiRISE observation.

**Figure 10.** Detections of monohydrated sulfate, polyhydrated material, and enhanced hydration in CRISM observations FRTC815 and FRTD26B showing the transition from the monohydrated state at the base to a polyhydrated state in the upper section. The location of Figure 11 is indicated by a yellow box.

*Massé et al.* [2008b] suggest that their continued existence can be explained by very slow transformation kinetics. The strongest ferric oxide and enhanced hydration detections occur on the slightly raised plateau in the northeast part of the deposit (Figures 2a and 2b), although hematite is detected in lower concentrations at slightly lower elevations due to erosion and transport onto lower-lying regions [*Glotch and Christensen*, 2005].

[22] In contrast to previous work, the analysis of high-resolution MRO data shows that this unit is unconformably superimposed on the monohydrated sulfate-bearing sedimentary section described in section 4.1. We see no evidence for polyhydrated signatures in these older deposits and we see no morphologic evidence that the polyhydrated deposits are beneath or included in the older deposits. For example, CRISM observations that cover parts of the older cliff-forming deposits (FRTC14E, FRTBE2D, and FRT7FA4) do not show spectral indications of polyhydrated sulfates in the wall exposures (Figure 9). In addition, examination of the cliff walls in CTX and HiRISE images show no indications of a low-albedo layer which might indicate the presence of polyhydrated/hematite/iron oxide material (Figure 11). Thus, even though this material is topographically below the cliff-forming unit (monohydrated sulfates and nanophase ferric oxides), we conclude the monohydrated sulfate-bearing unit was already emplaced and differentially eroded by the time the polyhydrated deposits formed. This inference is also consistent with mapping the spatial distribution of these materials using OMEGA data, morphology, and albedo [*Gendrin et al.*, 2005; *Noe Dobrea et al.*, 2008]. We infer that the polyhydrated deposits formed in local topographic lows after formation and differential erosion of the older, monohydrated sulfate-bearing sedimentary unit.

## 5. Summary and Implications

[23] Our work shows that the sedimentary deposits in Aram Chaos first formed with intercalated ferric hydroxysulfate ($Fe(OH)SO_4$) and monohydrated sulfates (likely, szomolnokite) at the base of the section, followed by monohydrated sulfates, followed by a mix of monohydrated sulfates and nanophase ferric oxides. The data show that these deposits were then differentially eroded by wind, after which polyhydrated materials (e.g., polyhydrated sulfates) with hematite and other ferric oxides were deposited in low-lying areas during a second depositional event. Work by *Wang and Freemen* [2009] shows that relative humidity is a critical factor in determining hydration/dehydration states of forming Mg sulfates. In conjunction with their work, our work indicates a possible change in environmental humidity between depositional events in Aram Chaos, beginning with the formation of ferric hydroxysulfate and monohydrated sulfate under relatively dry conditions and ending with the formation of polyhydrated materials under relatively wet conditions.

[24] We favor a formation mechanism involving groundwater recharge/evaporation and multiple wetting events to explain the stratigraphic section observed in the sedimentary deposits in Aram Chaos. Regional-scale groundwater distribution modeling by *Andrews-Hanna et al.* [2007] predicts Aram Chaos to have one of the thickest evaporite deposits in the region. A regional-scale groundwater system would link the deposits in Aram Chaos to those in Meridiani Planum to
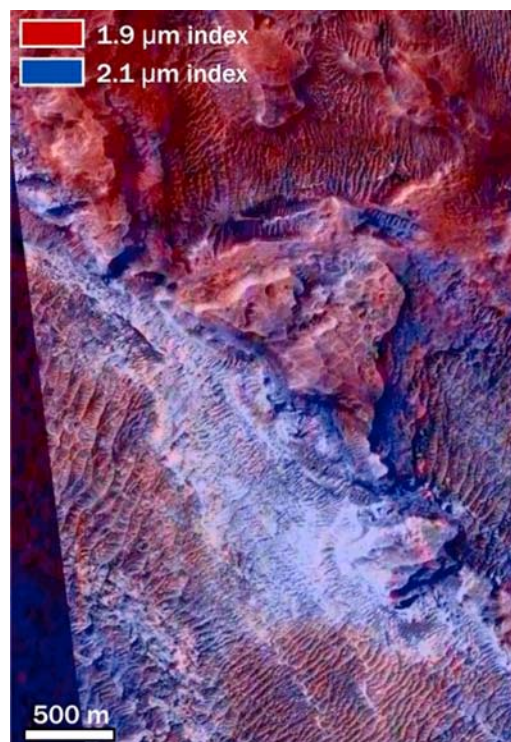


**Figure 11.** Subset of HiRISE image PSP_010025_1835 (center is at 3.39°N, 339.42°E). The monohydrated sulfate-bearing material is in layers at the base of the polyhydrated/hematite/ferric oxide unit. Aeolian ripples lying on top of the monohydrated material show an absorption at 1.9 $\mu$m, suggesting that it is material that has been eroded off the polyhydrated/hematite/ferric oxide unit. The ripples visible at the bottom of the image are trending SW-NE and are indicative of winds blowing predominantly from the northwest.

the east and Valles Marineris to the west, so evaporite deposits in these regions should show similarities to the deposits in Aram Chaos. Analysis of sulfate deposits in Meridiani [*Wiseman et al.*, 2010] shows that monohydrated and polyhydrated sulfate species in the northern valley are likely separated from the main Meridiani sequence by erosion, indicating a pause between depositional events in this area too. The sequence of polyhydrated sulfates overlying monohydrated sulfates is mimicked to the west in Candor Chasma, where *Murchie et al.* [2009] found that polyhydrated materials in Candor Chasma are younger than the monohydrated sulfates and occupy topographic lows. Both the sequence of polyhydrated materials overlying intercalated ferric hydroxysulfate and monohydrated sulfates and the unconformable contact between them signifying a period of erosion between depositional events in multiple locations throughout this region indicate that a plausible formation method is a series of groundwater upwelling events fed by groundwater recharge, as modeled by *Andrews-Hanna et al.* [2007].

## References

Andrews-Hanna, J. C., R. J. Phillips, and M. T. Zuber (2007), Meridiani Planum and the global hydrology of Mars, *Nature*, *446*, 163–166, doi:10.1038/nature05594.

Ansan, V., N. Mangold, P. Masson, and G. Neukum (2008), The topography of valley networks on Mars: Comparison between valleys of different ages, *Lunar Planet. Sci. [CD-ROM]*, *XXXIX*, abstract 1585.

Arvidson, R. E., et al. (2006), Nature and origin of the hematite-bearing plains of Terra Meridiani based on analyses of orbital and Mars Exploration rover data sets, *J. Geophys. Res.*, *111*, E12S08, doi:10.1029/2006JE002728.

Bishop, J. L., et al. (2009), Mineralogy of Juventae Chasma: Sulfates in the light-toned mounds, mafic minerals in the bedrock, and hydrated silica and hydroxylated ferric sulfate on the plateau, *J. Geophys. Res.*, *114*, E00D09, doi:10.1029/2009JE003352.

Carr, M. H. (1979), Formation of Martian flood features by release of water from confined aquifers, *J. Geophys. Res.*, *84*(B6), 2995–3007, doi:10.1029/JB084iB06p02995.

Christensen, P. R., R. V. Morris, M. D. Lane, J. L. Bandfield, and M. C. Malin (2001), Global mapping of Martial hematite mineral deposits: Remnants of water-driven processes on early Mars, *J. Geophys. Res.*, *106*(E10), 23,873–23,885, doi:10.1029/2000JE001415.

Cloutis, E. A., et al. (2006), Detection and discrimination of sulfate minerals using reflectance spectroscopy, *Icarus*, *184*, 121–157, doi:10.1016/j.icarus.2006.04.003.

Fenton, L. K., and M. I. Richardson (2001), Martian surface winds: Insensitivity to orbital changes and implications for aeolian processes, *J. Geophys. Res.*, *106*(E12), 32,885–32,902, doi:10.1029/2000JE001407.

Gendrin, A., et al. (2005), Sulfate in Martian layered terrains: The OMEGA/Mars Express view, *Science*, *307*, 1587–1591, doi:10.1126/science.1109087.

Glotch, T. D., and P. R. Christensen (2005), Geologic and mineralogic mapping of Aram Chaos: Evidence for a water-rich history, *J. Geophys. Res.*, *110*, E09006, doi:10.1029/2004JE002389.

Glotch, T. D., and A. D. Rogers (2007), Evidence for aqueous deposition of hematite- and sulfate-rich light-toned layered deposits in Aureum and Iani Chaos, Mars, *J. Geophys. Res.*, *112*, E06001, doi:10.1029/2006JE002863.

Grotzinger, J. P., et al. (2005), Stratigraphy and sedimentology of a dry to wet eolian depositional system, Burns formation, Meridiani Planum, Mars, *Earth Planet. Sci. Lett.*, *240*, 11–72, doi:10.1016/j.epsl.2005.09.039.

Langevin, Y., F. Poulet, J.-P. Bibring, and B. Gondet (2005), Sulfates in the north polar region of Mars detected by OMEGA/Mars Express, *Science*, *307*, 1584–1586, doi:10.1126/science.1109091.

Lichtenberg, K. A., et al. (2007), Coordinated analyses of orbital and Spirit Rover data to characterize surface materials on the cratered plains of Gusev Crater, Mars, *J. Geophys. Res.*, *112*, E12S90, doi:10.1029/2006JE002850.

Lichtenberg, K. A., R. E. Arvidson, J. L. Bishop, T. D. Glotch, E. Z. Noe Dobrea, S. L. Murchie, J. F. Mustard, L. H. Roach, and the CRISM Team (2008), Mg- and Fe-sulfate layers in Aram Chaos, Mars, *Eos Trans. AGU*, *89*(53), Fall Meet. Suppl., Abstract P44A-09.

Malin, M. C., et al. (2007), Context camera investigation on board the Mars Reconnaissance Orbiter, *J. Geophys. Res.*, *112*, E05S04, doi:10.1029/2006JE002808.

Massé, M., O. Bourgeois, S. Le Mouelic, L. Le Deit, C. Verpoorter, J. P. Combe, C. Sotin, J.-P. Bibring, B. Gondet, Y. Langevin, and The OMEGA Team (2008a), Sulfates, ferric oxides, and Al-OH bearing minerals in Aram Chaos: Comparison of OMEGA and CRISM data, paper presented at Workshop on Martian Phyllosilicates: Recorders of Aqueous Processes, Inst. Astrophys. Spatiale, Paris.

Massé, M., S. Le Mouélic, O. Bourgeois, J.-P. Combe, L. Le Deit, C. Sotin, J.-P. Bibring, B. Gondet, and Y. Langevin (2008b), Mineralogical composition, structure, morphology, and geological history of Aram Chaos crater fill on Mars derived from OMEGA Mars Express data, *J. Geophys. Res.*, *113*, E12006, doi:10.1029/2008JE003131.

McEwen, A. S., et al. (2007), Mars Reconnaissance Orbiter's High Resolution Imaging Science Experiment (HiRISE), *J. Geophys. Res.*, *112*, E05S02, doi:10.1029/2005JE002605.

Milliken, R. E., et al. (2008), Opaline silica in young deposits on Mars, *Geology*, *36*(11), 847–850, doi:10.1130/G24967A.1.

Morris, R. V., et al. (2000), Mineralogy, composition, and alteration of Mars Pathfinder rocks and soils: Evidence from multispectral, elemental, and magnetic data on terrestrial analogue, SNC meteorite, and Pathfinder samples, *J. Geophys. Res.*, *105*(E1), 1757–1817, doi:10.1029/1999JE001059.

Morris, R. V., et al. (2006a), Mössbauer mineralogy of rock, soil, and dust at Gusev crater, Mars: Spirit's journey through weakly altered olivine basalt on the plains and pervasively altered basalt in the Columbia Hills, *J. Geophys. Res.*, *111*, E02S13, doi:10.1029/2005JE002584.

Morris, R. V., et al. (2006b), Mössbauer mineralogy of rock, soil, and dust at Meridiani Planum, Mars: Opportunity's journey across sulfate-rich outcrop, basaltic sand and dust, and hematite lag deposits, *J. Geophys. Res.*, *111*, E12S15, doi:10.1029/2006JE002791.

Morris, R. V., et al. (2008), Iron mineralogy and aqueous alteration from Husband Hill through Home Plate at Gusev Crater, Mars: Results from the Mössbauer instrument on the Spirit Mars Exploration Rover, *J. Geophys. Res.*, *113*, E12S42, doi:10.1029/2008JE003201.

Murchie, S., et al. (2007), Compact Reconnaissance Imaging Spectrometer for Mars (CRISM) on Mars Reconnaissance Orbiter (MRO), *J. Geophys. Res.*, *112*, E05S03, doi:10.1029/2006JE002682.

Murchie, S., et al. (2009), Evidence for the origin of layered deposits in Candor Chasma, Mars, from mineral composition and hydrologic modeling, *J. Geophys. Res.*, *114*, E00D05, doi:10.1029/2009JE003343.

Mustard, J. F., F. Poulet, A. Gendrin, J.-P. Bibring, Y. Langevin, B. Gondet, N. Mangold, G. Bellucci, and F. Altieri (2005), Olivine and pyroxene diversity in the crust of Mars, *Science*, *307*, 1594–1597, doi:10.1126/science.1109098.

Neukum, G., R. Jaumann, and the HRSC Co-investigator and Experiment Team (2004), HRSC: The High Resolution Stereo camera of Mars Express, in *Mars Express—The Scientific Payload*, edited by A. Wilson, *Eur. Space Agency Spec. Publ.*, ESA SP-1240, 17–35.

Noe Dobrea, E. Z., F. Poulet, and M. C. Malin (2008), Correlations between hematite and sulfates in the chaotic terrain east of Valles Marineris, *Icarus*, *193*, 516–534, doi:10.1016/j.icarus.2007.06.029.

Nummedal, D., and D. B. Prior (1981), Generation of Martian chaos and channels by debris flows, *Icarus*, *45*, 77–86, doi:10.1016/0019-1035(81)90007-5.

Oosthoek, J. H. P., T. E. Zegers, A. Rossi, B. Foing, G. Neukum, and the HRSC Co-investigator Team (2007), 3D mapping of Aram Chaos: A record of fracturing and fluid activity, *Lunar Planet. Sci. [CD-ROM]*, *XXXVII*, Abstract 1577.

Pelkey, S. M., et al. (2007), CRISM multispectral summary products: Parameterizing mineral diversity in Mars from reflectance, *J. Geophys. Res.*, *112*, E08S14, doi:10.1029/2006JE002831.

Roach, L. H., J. F. Mustard, S. L. Murchie, J.-P. Bibring, F. Forget, K. W. Lewis, O. Aharonson, M. Vincendon, and J. L. Bishop (2009), Testing evidence of recent hydration state change in sulfates on Mars, *J. Geophys. Res.*, *114*, E00D02, doi:10.1029/2008JE003245.

Rodriguez, J. A. P., S. Sasaki, R. O. Kuzmin, J. M. Dohm, K. L. Tanaka, H. Miyamoto, K. Kurita, G. Komatsu, A. G. Fairen, and J. C. Ferris (2005), Outflow channel sources, reactivation, and chaos formation, Xanthe Terra, Mars, *Icarus*, *175*, 36–57, doi:10.1016/j.icarus.2004.10.025.

Smith, D. E., et al. (2001), Mars Orbiter Laser Altimiter: Experiment summary after the first year of global mapping of Mars, *J. Geophys. Res.*, *106*(E10), 23,689–23,722, doi:10.1029/2000JE001364.

Smith, D. E., G. A. Neumann, R. E. Arvidson, E. Guinness, and S. Slavney (2003), Mars Global Surveyor Laser Altimeter Mission Experiment Gridded Data Record, MGS-M-MOLA-5-MEGDR-L3-V1.0, http://pds-geosciences.wustl.edu/missions/mgs/megdr.html, NASA Planet. Data Syst., Saint Louis, Mo.

Squyres, S. W., et al. (2004), The Opportunity Rover's Athena science investigation at Meridiani Planum, Mars, *Science*, *306*, 1698–1703, doi:10.1126/science.1106171.

Tosca, N. J., and S. M. McLennan (2006), Chemical divides and evaporite assemblages on Mars, *Earth Planet. Sci. Lett.*, *241*, 21–31, doi:10.1016/j.epsl.2005.10.021.

Wang, A., and J. J. Freemen (2009), Pathways and rates of Mg-sulfate dehydration and rehydration on Mars, *Lunar Planet. Sci.* [CD-ROM], *XXXX*, Abstract 3034.

Wiseman, S. J., R. E. Arvidson, R. V. Morris, F. Poulet, J. C. Andrews-Hanna, J. L. Bishop, S. L. Murchie, F. P. Seelos, D. Des Marais, and J. L. Griffes (2010), Spectral and stratigraphic mapping of hydrated sulfate and phyllosilicate-bearing deposits in northern Sinus Meridiani, Mars, *J. Geophys. Res.*, doi:10.1029/2009JE003354, in press.

J. Andrews-Hanna, Department of Geophysics, Colorado School of Mines, Golden, CO 80401, USA.

R. E. Arvidson and K. A. Lichtenberg, McDonnell Center for the Space Sciences, Department of Earth and Planetary Sciences, Washington University, Saint Louis, MO 63130, USA. (lichtenberg@wunder.wustl.edu)

J. L. Bishop, SETI Institute, Mountain View, CA 94043, USA.

D. Fernandez Remolar, Centro de Astrobiología, INTA-CSIC, E-28850 Madrid, Spain.

T. D. Glotch, Department of Geosciences, State University of New York at Stony Brook, Stony Brook, NY 11794, USA.

R. V. Morris, NASA Johnson Space Center, Houston, TX 77058, USA.

S. L. Murchie, Johns Hopkins University Applied Physics Laboratory, Laurel, MD 20723, USA.

J. F. Mustard, Department of Geological Sciences, Brown University, Providence, RI 02912, USA.

E. Noe Dobrea, Planetary Science Institute, 1700 East Fort Lowell, Ste. 106, Tucson, AZ 85719, USA.

L. H. Roach, Frontier Technology, Inc., Beverly, MA 01915, USA.